Journal of Materials Science & Technology 146 (2023) 168–176

Contents lists available at ScienceDirect

Journal of Materials Science & Technology

journal homepage: www.elsevier.com/locate/jmst

Research Article

Giant low-field magnetocaloric effect in ferromagnetically ordered $Er_{1-x}Tm_xAl_2$ ($0 \le x \le 1$) compounds

Shuxian Yang[a,b], Xinqi Zheng[a,*], Dingsong Wang[a], Juping Xu[c,d], Wen Yin[c,d], Lei Xi[a,e], Chaofan Liu[a], Jun Liu[f], Jiawang Xu[g,b], Hu Zhang[a], Zhiyi Xu[b,h], Lichen Wang[h,i], Yihong Yao[a], Maosen Zhang[a], Yichi Zhang[a], Jianxin Shen[a], Shouguo Wang[a,e,*], Baogen Shen[b,h,i]

[a] School of Materials Science and Engineering, Beijing Advanced Innovation Center for Materials Genome Engineering, University of Science and Technology Beijing, Beijing 100083, China
[b] Beijing National Laboratory for Condensed Matter Physics, Institute of Physics, Chinese Academy of Sciences & University of Chinese Academy of Sciences, Beijing 100190, China
[c] Institute of High Energy Physics, Chinese Academy of Sciences, Beijing 100049, China
[d] Spallation Neutron Source Science Center, Dongguan 523803, China
[e] School of Materials Science and Engineering, Anhui University, Hefei 230601, China
[f] Department of Energy and Power Engineering, School of Mechanical Engineering, Beijing Institute of Technology, Beijing 100081, China
[g] Songshan Lake Materials Laboratory, Dongguan 523808, China
[h] Ganjiang Innovation Academy, Chinese Academy of Sciences, Ganzhou 341000, China
[i] Ningbo Institute of Materials Technology and Engineering, Chinese Academy of Sciences, Ningbo 315201, China

ARTICLE INFO

Article history:
Received 31 July 2022
Revised 19 October 2022
Accepted 20 October 2022
Available online 23 December 2022

Keywords:
Magnetocaloric effect
Low field magnetocaloric effect
Magnetic structure
RAl_2 compounds

ABSTRACT

Magnetocaloric material is the key working substance for magnetic refrigerant technology, for which the low-field and low-temperature magnetocaloric effect (MCE) performance is of great importance for practical applications at low temperatures. Here, a giant low-field magnetocaloric effect in ferromagnetically ordered $Er_{1-x}Tm_xAl_2$ ($0 \le x \le 1$) compounds was reported, and the magnetic structure was characterized based on low-temperature neutron powder diffraction. With increasing Tm content from 0 to 1, the Curie temperature of $Er_{1-x}Tm_xAl_2$ ($0 \le x \le 1$) compounds decreases from 16.0 K to 3.6 K. For $Er_{0.7}Tm_{0.3}Al_2$ compound, it showed the largest low-field magnetic entropy change ($-\Delta S_M$) with the peak value of 17.2 and 25.7 J/(kg K) for 0–1 T and 0–2 T, respectively. The $(-\Delta S_M)_{max}$ up to 17.2 J/(kg K) of $Er_{0.7}Tm_{0.3}Al_2$ compound for 0–1 T is the largest among the intermetallic magnetocaloric materials ever reported at temperatures below 20 K. The peak value of adiabatic temperature change $(\Delta T_{ad})_{max}$ was determined as 4.13 K and 6.87 K for 0–1 T and 0–2 T, respectively. The characteristic of second-order magnetic transitions was confirmed on basis of Arrott plots, the quantitative criterion of exponent n, rescaled universal curves, and the mean-field theory criterion. The outstanding low-field MCE performance with low working temperatures indicates that $Er_{1-x}Tm_xAl_2$ ($0 \le x \le 1$) compounds are promising candidates for magnetic cooling materials at liquid hydrogen and liquid helium temperatures.

1. Introduction

Magnetic refrigeration technology based on the theoretical foundation of magnetocaloric effect (MCE) has become an attractive alternative to conventional gas cooling methods due to its high efficiency and environmental friendliness [1–3]. Magnetocaloric material is one of the crucial parts for the practical development of magnetic refrigeration and it is usually evaluated by magnetic entropy change (ΔS_M), working temperature span (δT_{FWHM}), refrigeration capacity (RC), and adiabatic temperature change (ΔT_{ad}). Magnetic materials showing large MCE at low temperatures have potential applications for gas liquefaction such as helium (4.2 K), hydrogen (20 K), and nitrogen (77 K) [4,5]. In addition, the magnetocaloric materials with large MCE under low magnetic field change exhibit more applicable advantages because the magnetic field obtained from the permanent magnet is usually not more than 2 T for practical magnetic refrigerators. Furthermore, magnetocaloric materials with second-order magnetic phase transition are more advantageous for practical applications for good thermal and magnetic reversibility. Therefore, it is of significant importance

* Corresponding authors.
E-mail addresses: zhengxq@ustb.edu.cn (X. Zheng), sgwang@ustb.edu.cn (S. Wang).

https://doi.org/10.1016/j.jmst.2022.10.066
1005-0302/

to explore good magnetocaloric materials with low working temperatures, large low-field MCE, and second-order phase transition characteristics. Under this background, a lot of rare-earth-based intermetallic compounds with high MCE performance have been reported such as HoB_2, EuS, $Tm_{0.85}Ho_{0.15}Ga$, $Er_{0.9}Ho_{0.1}Ni$, TmCuAl, and TmCoSi [6–11]. However, low-field MCE performance should be further improved for practical applications.

Binary rare-earth-based RAl_2 (R-rare earth) compounds have $MgCu_2$-type cubic Laves phase crystal structure and show low magnetic ordering temperatures with complex magnetic properties [12,13]. $ErAl_2$ compound undergoes only one ferromagnetic (FM) to paramagnetic (PM) transition with Curie temperature (T_C) of ~14 K [14,15], and the value of T_C can be adjusted to the suitable temperature region by R-substitution [16–20]. For example, by Ho substitution, T_C of $Er_{1-x}Ho_xAl_2$ compounds is increased from 13 K to 32 K as x is increased from 0 to 1 [19]. Some works have also been reported on the MCE of the RAl_2 family [13,18,21–23], among which the $ErAl_2$ compound exhibits large $(-\Delta S_M)_{max}$ with the value of 22.6 and 36.2 J/(kg K) for 0–2 and 0–5 T, respectively [15,24]. The substitution of Pr, Tb, and Dy for Er on MCE was investigated, where the peak on $(-\Delta S_M)$ curves was found to move towards higher temperatures with increasing substitution content for the above situations [16–18]. However, almost no report was found to successfully move the peak temperature towards lower ranges or to increase the value of $-\Delta S_M$. The above two aspects are of great importance for the applications of low-temperature magnetic refrigeration. It is well known that atom-substitution is not only an effective way to adjust magnetic transition temperatures but also a powerful method to optimize MCE [25], because $(-\Delta S_M)_{max}$ is positively associated with magnetic moments but negatively associated with transition temperatures [26]. Spin angular momentum quantum number (S) plays a leading role in magnetic exchange actions for rare-earth-based intermetallic systems and it has been proved that it is positively related to magnetic ordering temperature [27]. Since Tm atoms have smaller S, it is expected to obtain larger MCE at lower temperatures by substitution of Tm for Er atom in $Er_{1-x}Tm_xAl_2$ compounds.

In this work, polycrystalline $Er_{1-x}Tm_xAl_2$ compounds were synthesized and the influence of Tm-substitution on crystal structure, magnetic structure, magnetic transition behavior, magnetic entropy change, and adiabatic temperature change was investigated by neutron powder diffraction and X-ray diffraction technique, magnetic measurements, and heat capacity measurements, respectively. Giant low-field magnetic entropy change was observed at low temperatures and the related physical mechanism was discussed.

2. Experimental methods

A series of polycrystalline $Er_{1-x}Tm_xAl_2$ ($0 \le x \le 1$) compounds were synthesized by arc-melting stoichiometric amounts of the constituent elements in an argon atmosphere, using a water-cooled copper bottom block. Due to volatilization, 2% of Er and Tm was over-added into the stoichiometric amounts of the mixture before melting. The purity of Al and rare-earth metals was higher than 99.9%. The ingots were turned over several times to ensure homogeneity. The samples were then annealed at 873 K for 3 weeks, and a subsequent quenching in liquid nitrogen was finally performed. The annealed samples were ground into powder and the phase purity together with crystal structure was examined by powder X-ray diffraction (XRD) experiments with Cu-Kα radiation (wavelength λ = 1.5406 Å) measured at a step of 0.02°. The Rietveld refinement analysis was performed by using the program of GSAS. The morphology and component of the sample were measured by using a backscattering detector (BSD) and a field-emission scanning electron microscope (SEM, Phenom Pro-X) equipped with an energy-dispersive X-ray spectrometer (EDS). The element analysis was performed with both modes of area mapping with a view field of 17.9 μm and line scanning with a resolution of 512 points.

Neutron powder diffraction (NPD) measurements were performed at 5 K on the multi-physics instrument (MPI) at the China Spallation Neutron Source (CSNS). Samples were loaded in 9.0 mm vanadium cans and diffraction patterns were collected in the time-of-flight (T. O. F.) mode with wavelength bands of 0.1–4.5 Å. The low temperature of 5 K was achieved with cryostat (CCR06) and the sample was kept at 5 K for 30 min before measurements. The program of GSAS was used for the Rietveld refinement of NPD patterns. The magnetic measurements were performed on the vibrating sample magnetometer with quantum design (SQUID-VSM) and Physical Property Measurement System (PPMS). Isothermal magnetization measurements were carried out in stable mode at each point. The oscillatory demagnetization was performed before isothermal magnetization measurements to eliminate the influence of residual magnetization. The shape of the sample for magnetic measurements is near-spherical and the effect of self-demagnetization was taken into account with the self-demagnetization factor of 1/3. Specific heat measurements were carried out also by using PPMS. The final heat capacity data was obtained by subtracting the data of the sample holder together with glue from the total measured data.

3. Results and discussion

The powder XRD measurements were performed with 2θ from 10° to 90° at room temperature for all the samples and the diffraction patterns were analyzed by the Rietveld refinement method. As a representative, the experimental XRD pattern together with fitting curves of the $Er_{0.7}Tm_{0.3}Al_2$ compound was plotted in Fig. 1(a). All the main peaks can be indexed to the standard Bragg positions of RAl_2 compounds as marked at the bottom of the picture. Though there are extra peaks around 29 and 31°, the $Er_{0.7}Tm_{0.3}Al_2$ compound is still considered as a pure phase because the extra peaks are very weak. The fitting error was calculated to be wRp = 4.4% and Rp = 2.9%. Rietveld analysis further indicates that $Er_{1-x}Tm_xAl_2$ ($0 \le x \le 1$) compounds have $MgCu_2$-type cubic Laves phase structure (space group $Fd3\_m$), in good accordance with reported results of RAl_2 compounds [28]. The crystal structure was presented in the inset of Fig. 1(a). The lattice parameter a and volume (V) were determined to be 7.7877(1) Å and 471.313(7) Å^3, respectively. Similar results were obtained for all $Er_{1-x}Tm_xAl_2$ compounds. Moreover, the lattice parameter a and V as a function of Tm-content were plotted in Fig. 1(b, c), respectively. An approximatively linear relationship between parameter a and Tm concentration indicates that the chemical compositions of as-prepared samples are close to the desired contents according to Vegard's law [29,30]. In addition, the monotonic decreasing trend between V and Tm-content can be found, which arises from the fact that the radius of Tm atoms is smaller than that of Er atoms according to lanthanide contraction law. The above results also confirm that Tm-substitution makes no change in crystal structure and symmetry, but with a little variation of detailed lattice parameters.

In order to investigate the phase homogeneity and phase components, the morphology of the $Er_{0.7}Tm_{0.3}Al_2$ compound was examined by SEM and the picture was presented in Fig. 2(a). It can be seen that the contrast is almost uniform except for several scratches in the whole field of view, indicating good homogeneity. Then the element distribution was investigated according to area mapping and line scanning based on EDS analysis. The distributions of Er, Tm, and Al elements in the view field of 17 μm were presented in Fig. 2(b–d), respectively. It can also be seen that these elements are nearly uniformly distributed in each part of the measured sample, which further confirms the homogeneity of

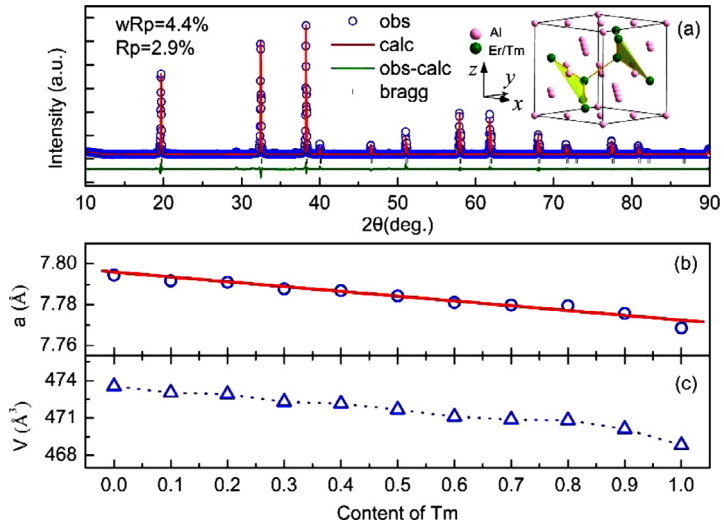

Fig. 1. (a) Rietveld refinement powder XRD pattern of $Er_{0.7}Tm_{0.3}Al_2$ compound at room temperature. Inset: crystal structure of $Er_{1-x}Tm_xAl_2$ compounds. (b) Tm-content dependence of lattice parameters a for $Er_{1-x}Tm_xAl_2$ ($0 \le x \le 1$) compounds. (c) Tm-content dependence of lattice parameters V for $Er_{1-x}Tm_xAl_2$ ($0 \le x \le 1$) compounds.

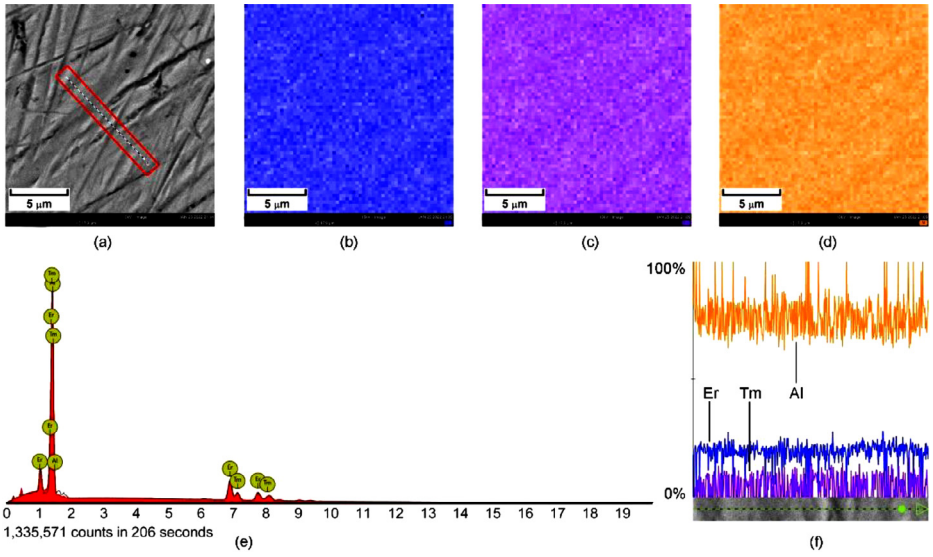

Fig. 2. (a) Field of view for area mapping and the range for line scanning as indicated by the red box for the $Er_{0.7}Tm_{0.3}Al_2$ compound. Distribution of (b) Er, (c) Tm, and (d) Al elements based on area mapping. (e) EDS data of $Er_{0.7}Tm_{0.3}Al_2$ compound. (f) Atomic ratio of Er, Tm, and Al elements at different points with line scanning.

the $Er_{0.7}Tm_{0.3}Al_2$ compound. Furthermore, the component of the $Er_{0.7}Tm_{0.3}Al_2$ compound can also be investigated based on the EDS data as shown in Fig. 2(e). The atomic ratio of Er:Tm:Al according to area mapping was calculated as 20.83:9.15:70.02. Line scanning was also performed in the range indicated by the red box as marked in Fig. 2(a). The position dependences of atomic ratio for Er, Tm, and Al were all presented in Fig. 2(f). The average atomic ratio of Er:Tm:Al according to line scanning was determined to be 20.53:9.11:70.36. The above results from area mapping and line scanning are both close to the nominal component with a ratio of 23.33:9.99:66.67. The SEM experiments and related analysis indicate that no component segregation exists in the $Er_{0.7}Tm_{0.3}Al_2$ compound and the sample has good purity of phase.

The magnetic ordering of Er atoms in the $ErAl_2$ compound was described as FM and the easy axis of magnetization is along ⟨111⟩ in Refs. [19,31,32]. However, the magnetic structure has never been detected directly and the detail of ordered magnetic moments is unclear. As a representative, the magnetic structure of the $Er_{0.7}Tm_{0.3}Al_2$ compound was characterized by neutron powder diffraction (NPD) experiments at 5 K. The interplanar crystal spacing (d) dependence of the diffraction intensity curve, Rietveld refinement curve, and the difference between them were shown in Fig. 3(a). It can be seen that the fitting between experimental data and calculated points is very good, where the fitting error is calculated as $wRp = 4.31\%$ and $Rp = 3.94\%$. It is known that neutrons can be scattered not only by periodically arranged atomic nuclei but also by periodically arranged atomic magnetic moments. Based on the above principles, crystal structure and magnetic structure can be well resolved according to NPD data. In order to distinguish the diffraction signals from the crystal structure and magnetic structure, the calculated curves attributed to them together with the corresponding Bragg positions were presented in Fig. 3(b, c), respectively. It is found that the $Er_{0.7}Tm_{0.3}Al_2$ compound has a cubic structure with space group $Fd3\_m$ (NO. 227), and rare earth atoms (Er and Tm) and Al atoms occupy 8b and 16c sites with site symmetry of ($\bar{4}$ 3 m) and (. $\bar{3}$ m) correspondingly. The crystal structure for the $Er_{0.7}Tm_{0.3}Al_2$ compound at 5 K is the same as that at room temperature (300 K), indicating that no structure transition takes place with increasing temperature. It can also be seen that the Bragg positions of the crystal structure are in good accordance

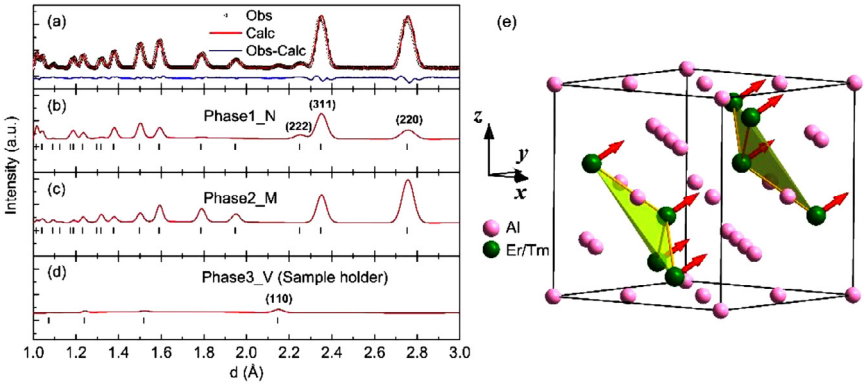

Fig. 3. (a) NPD pattern of $Er_{0.7}Tm_{0.3}Al_2$ compound at 5 K, Rietveld refinement to the experimental data, and the difference between observed data and calculated data. (b) Contribution of crystal structure on NPD pattern from $Er_{0.7}Tm_{0.3}Al_2$ compound. (c) Contribution of magnetic structure on NPD pattern from R atoms. (d) Contribution of crystal structure on NPD pattern from sample holder vanadium. (e) Schematic picture of magnetic structure for $Er_{0.7}Tm_{0.3}Al_2$ compound at 5 K.

with those of the magnetic structure. It indicates that the unit cell of the crystal structure is the same as that of magnetic structure and thus FM order is expected to exist in the $Er_{0.7}Tm_{0.3}Al_2$ compound. Furthermore, obvious magnetic signals were observed around d = 2.75 and 2.35 Å corresponding to crystallographic planes (220) and (311) respectively. However, no magnetic signal was observed around d = 2.25 Å corresponding to the crystallographic plane (222). The above data indicate that the projection of long-range ordered magnetic moments on crystal faces (220) and (311) is quite large but that on crystal face (222) is almost zero. Actually, both the direction and magnitude of the ordered magnetic moments can be obtained in detail according to Rietveld refinement and the magnetic structure for $Er_{0.7}Tm_{0.3}Al_2$ compound at 5 K was schematically shown in Fig. 3(e). It shows that the magnetic moments are ferromagnetically ordered along the crystallographic direction ⟨111⟩ with an average value of 7.5 μ_B. Since crystallographic direction ⟨111⟩ is perpendicular to the crystal face (222), thus no magnetic peak can be observed on (222). The resolved magnetic structure is in good agreement with the report of easy axis for the $ErAl_2$ compound, because the direction of the magnetic moments described in the magnetic structure is just the direction of spontaneous magnetization [19,31,32]. It should be noticed that Er and Tm atoms are not treated separately in the magnetic structure model during fitting and the obtained average value is close to the theoretical value of 8.4 μ_B. The uniformity of magnetic ordering direction and the easy axis of ⟨111⟩ indicates that the $Er_{0.7}Tm_{0.3}Al_2$ compound can be magnetized easily by the external magnetic field. Finally, the peak around d = 2.15 Å could not be indexed to the crystal structure or the magnetic structure of the $Er_{0.7}Tm_{0.3}Al_2$ compound as shown in Fig. 3(d). According to further analysis, this signal was identified as the crystal plane (110) of vanadium metal from a sample holder made of vanadium elementary substance.

The temperature-dependent magnetization measurements were performed to investigate the magnetic transition for $Er_{1-x}Tm_xAl_2$ ($0 \le x \le 1$) compounds. Zero-field-cooling (ZFC) and field-cooling (FC) curves under the applied field of 0.01 T were presented in Fig. 4(a) for the $Er_{0.7}Tm_{0.3}Al_2$ compound as a representative. Firstly, the typical behavior of a ferromagnet with one sharp decrease of magnetization with increasing temperature is observed, which indicates that FM-PM transition takes place at Curie temperature (T_C), in good accordance with the reported results of $ErAl_2$ [14]. The value of T_C can be determined by the temperature corresponding to the minimum of dM/dT here [5]. It is noteworthy that ZFC and FC curves are overlapped well above T_C, indicating that there is no thermal hysteresis as that usually observed in second-order magnetic transition materials [10], which will be further discussed later. Secondly, the obvious difference between the ZFC and FC curves observed at low temperatures below T_C may be due to the domain-wall pinning effect [33]. That is because the magnetic atoms show non-negligible magneto-crystalline anisotropy and the magnetic domains were frozen during the zero-field cooling process. When a magnetic field not large enough was applied, the domain wall couldn't move freely. And when a larger magnetic field was applied, the domain wall can move easily and the bifurcation will disappear. The temperature dependence of reciprocal magnetic susceptibility (χ^{-1}) in the PM region obeys the Curie–Weiss law $\chi^{-1} = (T - \theta_P)/C$ for all compounds, where the linear fitting for $Er_{0.7}Tm_{0.3}Al_2$ is presented in inset of Fig. 4(a). In addition, the effective magnetic moment (μ_{eff}) was calculated to be 8.6 μ_B, close to the theoretical value of 8.9 μ_B for the weighted average of Er^{3+} and Tm^{3+} magnetic moments. The value of T_C as a function of Tm content was presented in Fig. 4(b). It is obvious that T_C decreases from 16.0 to 3.6 K monotonically with increasing x from 0 to 1, indicating that Tm substitution makes a significant influence on magnetic ordering temperature for $Er_{1-x}Tm_xAl_2$ ($0 \le x \le 1$) compounds. Generally speaking, the order-to-disorder magnetic transition originates from the competition between magnetic exchange interaction and thermal vibration. The spin of R atoms plays a dominant role in the magnetic exchange interaction and thus T_C is closely correlated with Spin in $Er_{1-x}Tm_xAl_2$ compounds [26,27]. Since the value of Spin for Tm is smaller than that for Er, Tm-substitution leads to a monotonic decrease of T_C. Similar phenomena and interpretations about the variation of T_C were reported for $Er_{1-x}Ho_xNi$ and $Ho_{1-x}Dy_xB_2$ systems [9,34].

Detailed isothermal magnetization (MH) curves under magnetic fields up to 7 T were also measured at the temperatures from 5 K to 60 K for $Er_{1-x}Tm_xAl_2$ compounds, where the typical curves of $Er_{0.7}Tm_{0.3}Al_2$ were shown in Fig. 4(c). It can be clearly seen that the magnetization increases sharply with increasing magnetic fields, then shows a slow increase, and finally reaches saturation at temperatures below T_C. This is the typical characteristic of the FM ground state, similar to the reported $ErAl_2$ compound [15]. It should be noted that not only the ground state of the $Er_{0.7}Tm_{0.3}Al_2$ compound is FM, but also the saturation field of it is very low. It indicates that the $Er_{0.7}Tm_{0.3}Al_2$ compound can be easily magnetized, which is in accord with the result of FM ordering and will have an important influence on MCE. At temperatures far higher than T_C, for example, 60 K, the field dependence of the magnetization exhibits a linear relation, which is typical for the PM state. The isothermal magnetization curves at the temperatures above but near T_C show a slight curvature, indicating the existence of short-range FM orders at these temperatures. Based on the above analysis, it further indicates that the $Er_{0.7}Tm_{0.3}Al_2$ compound un-

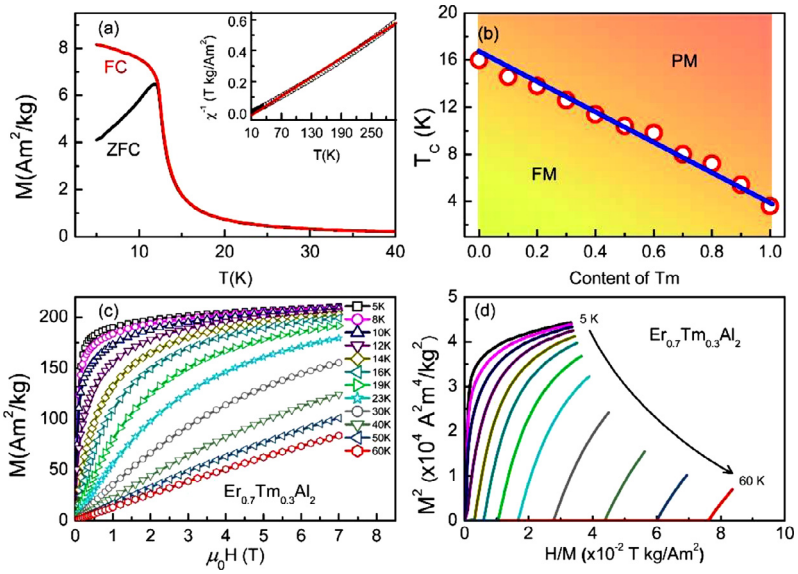

Fig. 4. (a) ZFC and FC curves with a field of 0.01 T for $Er_{0.7}Tm_{0.3}Al_2$. Inset: the relationship between temperature and reciprocal susceptibility. (b) T_C as a function of Tm content for $Er_{1-x}Tm_xAl_2$ ($0 \le x \le 1$) compounds. (c) Isothermal magnetization curves and (d) Arrott plots at temperatures from 5 K to 60 K with applied fields up to 7 T for $Er_{0.7}Tm_{0.3}Al_2$.

Table 1
Magnetic transition temperatures and MCE parameters under the field changes of 0–1 T, 0–2 T, and 0–5 T for $Er_{1-x}Tm_xAl_2$ compounds and some representative low-temperature refrigerant materials.

Samples	T_C (K)	$(-\Delta S_M)_{max}$ (J/(kg K)) 0–1 T	0–2 T	0–5 T	ΔT_{ad} (K) 0–1 T	0–2 T	0–5 T	Refs.
EuS	18.2	13.5 [a]	22.0	37.0		7.5	10.4	[7]
HoB_2	15.0	14.9[a]	24.1[a]	40.1	3.4	6.0	12.0	[6]
TmGa	15.0	12.9	20.6	34.2	3.2	5.0	9.1	[38]
$ErMn_2Si_2$	6.6	14.7	20.0	25.2	2.5	5.4	12.9	[39]
ErNiBC	5.0	9.8	16.8	24.8	2.7	5.3	8.6	[40]
TmCoSi	4.4	12.0	17.5 [a]	22.1	6.2		17.3	[11]
TmCuAl	4.0	12.2	17.2	24.3		4.6	9.4	[10]
$ErAl_2$	14.0		22.6 [a]	36.2 [a]		5.5 [a]	11.1[a]	[24]
$ErAl_2$	16.0	15.6	23.9	36.6				This work
$Er_{0.9}Tm_{0.1}Al_2$	14.6	14.8	22.5	35				This work
$Er_{0.8}Tm_{0.2}Al_2$	13.8	15.4	22.9	33.8				This work
$Er_{0.7}Tm_{0.3}Al_2$	12.6	17.2	25.7	37.1	4.13	6.87	12.43	This work
$Er_{0.6}Tm_{0.4}Al_2$	11.4	16.7	24.7	35.3	4.06	6.91	12.73	This work
$Er_{0.5}Tm_{0.5}Al_2$	10.4	13.9	20.8	30.3				This work
$Er_{0.4}Tm_{0.6}Al_2$	9.8	12.8	19.4	29.2				This work
$Er_{0.3}Tm_{0.7}Al_2$	8.0	14.7	21.4	30.7				This work
$Er_{0.2}Tm_{0.8}Al_2$	7.2	16.1	22.7	32.5				This work
$Er_{0.1}Tm_{0.9}Al_2$	5.4	14.1	20.3	31.8				This work
$TmAl_2$	3.6	13.1	19.8	34.8				This work

[a] These values were estimated from the relevant references.

dergoes FM-to-PM transition with increasing temperature. Furthermore, the Arrott plots for the $Er_{0.7}Tm_{0.3}Al_2$ compound were obtained based on isothermal magnetization data, which was presented in Fig. 4(d). The positive slope around T_C suggests the second-order characteristic of magnetic transition [35]. The results also prove that there is no volume/symmetry change accompanied by FM-to-PM transition because the magneto-structural transition is usually manifested as a first-order magnetic transition as reported previously [36].

The MCE was then evaluated by the isothermal magnetic entropy change (ΔS_M) for $Er_{1-x}Tm_xAl_2$ ($0 \le x \le 1$) compounds, which can be calculated from the experimental isothermal magnetization data by the Maxwell relation: $\Delta S_M = \int_0^H (\partial M/\partial T)_H dH$ [37].

The transition temperatures together with MCE parameters of $Er_{1-x}Tm_xAl_2$ compounds were listed in Table 1, and the $-\Delta S_M$ curves of $Er_{0.7}Tm_{0.3}Al_2$ compound as a function of temperature under different magnetic field changes were presented in Fig. 5(a). Only one prominent $-\Delta S_M$ peak can be observed in the vicinity of T_C corresponding to the contribution of FM-to-PM magnetic transition, and no obvious asymmetric broadening towards high temperatures was observed with increasing field change. It is different from typical Laves-phase magnetocaloric materials such as $ErCo_2$ compound because the magnetic transition of this series is second order while it is first order for $ErCo_2$ compound. However, it should still be noticed that the $-\Delta S_M$ peak moves to higher temperatures slightly with applied fields higher than 5 T, which can be attributed to the field-induced short-range FM order to long-range FM order transition in the PM region [38]. The maximal value of magnetic entropy change ($(-\Delta S_M)_{max}$) was calculated to be 17.2, 25.7, and 37.1 J/(kg K) for the field change of 0–1 T, 0–2 T, and 0–5 T, respectively. More importantly, the $(-\Delta S_M)_{max}$ for $Er_{0.7}Tm_{0.3}Al_2$ was significantly enhanced compared with the parent $ErAl_2$ compound, where the comparison between them was displayed in Fig. 5(b). The value of $(-\Delta S_M)_{max}$ increases quickly at low fields and then gradually reaches a saturation value of about

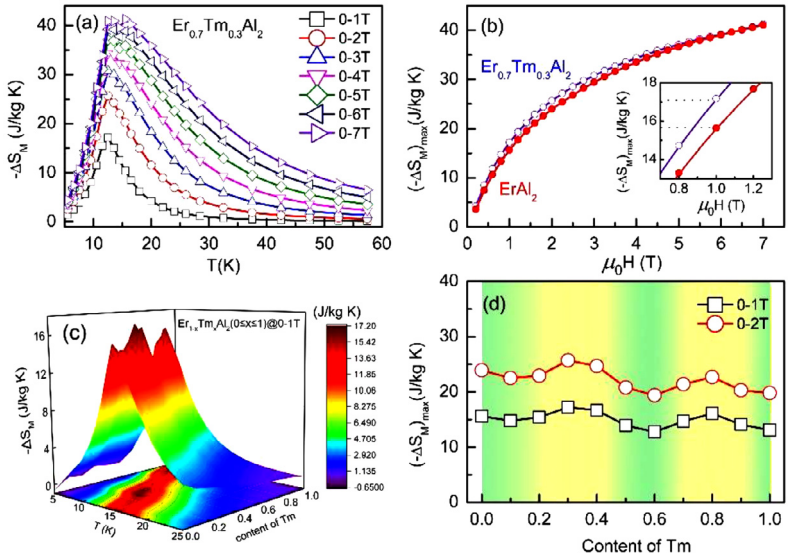

Fig. 5. (a) Temperature dependence of magnetic entropy change ($-\Delta S_M$) under different applied magnetic fields from 0–1 T to 0–7 T for $Er_{0.7}Tm_{0.3}Al_2$. (b) $(-\Delta S_M)_{max}$ as a function of applied magnetic fields for $Er_{0.7}Tm_{0.3}Al_2$ and parent $ErAl_2$ compound. Inset: enlarged view of comparison at low fields around 1 T. (c) ($-\Delta S_M$) as functions of temperature and the content of Tm for $Er_{1-x}Tm_xAl_2$ ($0 \le x \le 1$) compounds under the field change of 0–1 T. (d) The composition dependence of $(-\Delta S_M)_{max}$ under the field changes of 0–1 T and 0–2 T, respectively.

41.2 J/(kg K) with further increasing fields for both compounds. However, the $Er_{0.7}Tm_{0.3}Al_2$ compound exhibits larger values than $ErAl_2$ in the full range of field change up to 0–7 T, where an enlarged view of comparison at low fields is plotted in the inset of Fig. 5(b). $Er_{0.7}Tm_{0.3}Al_2$ compound shows a great enhancement by 10.3% on the $(-\Delta S_M)_{max}$ for the field change of 0–1 T compared with $ErAl_2$, where the $(-\Delta S_M)_{max}$ is determined to be 15.6 J/(kg K). Since the practical applied magnetic field is usually less than 2 T, the $Er_{0.7}Tm_{0.3}Al_2$ compound shows more potential applications than their parent alloys.

In addition, Tm substitution has a great influence on the shape of $-\Delta S_M$–T curves and the value of $(-\Delta S_M)_{max}$. Three-dimensional plots of Tm-content together with temperature dependences of $(-\Delta S_M)$ for $Er_{1-x}Tm_xAl_2$ ($0 \le x \le 1$) compounds with the field change of 0–1 T were shown in Fig. 5(c). On one hand, all of the curves for each component show only one peak, and the peaks move towards lower temperatures gradually with increasing Tm content. This shift of peak position comes from the variation of T_C, which shows a monotonic change with increasing Tm content. On the other hand, it should also be noted that the value of $(-\Delta S_M)_{max}$ shows a non-monotonic change with Tm content presented in Fig. 5(d), where two maximum values appear around $x = 0.3$ and $x = 0.8$, respectively. Actually, $(-\Delta S_M)_{max}$ can be approximately described by Eq. (1):

$$(-\Delta S_M)_{max} \approx 1.07nR\left(\frac{g\mu_B JH}{kT_0}\right)^{2/3} \quad (1)$$

where n, R, g, J, k, and T_0 is the mole number, the universal gas constant, Lande factor, total angular momentum quantum number, Boltzmann constant, and ordering temperature, respectively. As a result, the value of $(-\Delta S_M)_{max}$ is negatively correlated with an order-to-disorder transition temperature (for example, T_C) and positively correlated with saturation magnetic moments which is exactly related to gJ according to Oesterreicher and Parker [26]. It has been discussed that T_C and Spin are positively correlated in $Er_{1-x}Tm_xAl_2$ compounds. The value of gJ is 9 and 7 for Er and Tm atoms, respectively. It is clear that both the numerator and denominator of the equation show a monotonic decrease with increasing Tm content, thus it is difficult to predict the trend of $(-\Delta S_M)_{max}$ for $Er_{1-x}Tm_xAl_2$ compounds. As a result, the value of $(-\Delta S_M)_{max}$ shows a serrated variation as presented in Fig. 5(d) and Table 1. Actually, the composition dependence of magnetization at 1 T has a similar variation trend to $(-\Delta S_M)_{max}$. Although causation couldn't be obtained between magnetization and magnetic entropy change, this result helps to understand the non-monotonous variation and two maxima. Furthermore, the sharpness of magnetization with temperature is also positively related to the $(-\Delta S_M)_{max}$ according to Maxwell relation. Taking the composition dependence of $|dM/dT|_{max}$ at 1 T as an example, two maximum values are observed as well at $x = 0.3$ and $x = 0.8$. It is also found that the obtained value of $(-\Delta S_M)_{max}$ for $ErAl_2$ is slightly larger than that reported previously under the field changes of 0–2 and 0–5 T [24]. Moreover, it is worth pointing out that the values of $(-\Delta S_M)_{max}$ for all $Er_{1-x}Tm_xAl_2$ compounds are larger than 12.8 J/(kg K) under the field change of 0–1 T, showing great competitiveness among low-temperature magnetocaloric materials. The best performance was observed for $Er_{0.7}Tm_{0.3}Al_2$ and $Er_{0.6}Tm_{0.4}Al_2$ compounds with $(-\Delta S_M)_{max}$ of 17.2 and 16.7 J/kg K, respectively. Besides, the value of $(-\Delta S_M)_{max}$ for other components is still larger than 15 J/(kg K) such as 15.4 and 16.1 J/(kg K) for $Er_{0.8}Tm_{0.2}Al_2$ and $Er_{0.2}Tm_{0.8}Al_2$ under field change of 0–1 T, respectively.

In order to compare the MCE performance between $Er_{1-x}Tm_xAl_2$ compounds and other reported magnetocaloric materials with working temperatures below 20 K, detailed MCE parameters were listed in Table 1, together with the comparison of $(-\Delta S_M)_{max}$ presented in Fig. 6. The excellent MCE performance of $Er_{0.7}Tm_{0.3}Al_2$ can be comparable or even much better than the best refrigerant materials for low-temperature applications. For example, the HoB_2 compound shows giant MCE at low temperatures with T_C of 15 K and the $(-\Delta S_M)_{max}$ is as high as 40.1 J/(kg K) for the field change of 0–5 T [6]. Although the $(-\Delta S_M)_{max}$ of $Er_{0.7}Tm_{0.3}Al_2$ compound for 0–5 T (37.1 J/(kg K)) is slightly smaller than that of HoB_2, the value of $(-\Delta S_M)_{max}$ for 0–1 T and 0–2 T (17.2, 25.7 J/(kg K)) is greatly larger than that of HoB_2 (~14.9, ~24.1 J/(kg K)). The $Er_{0.7}Tm_{0.3}Al_2$ compound also shows some advantages on the low-field $(-\Delta S_M)_{max}$ compared with EuS [7], TmGa [38], $ErMn_2Si_2$ [39], ErNiBC [40], TmCuAl [10], TmCoSi [11], HoCuAl [41], HoCuSi [42], $GdCoC_2$ [43], $TmMn_2Si_2$ [44], TmZn [45], and HoNiSi [46] (Table l and Fig. 6). As a matter of fact, the remarkable $(-\Delta S_M)_{max}$ under field change of 0–1 T

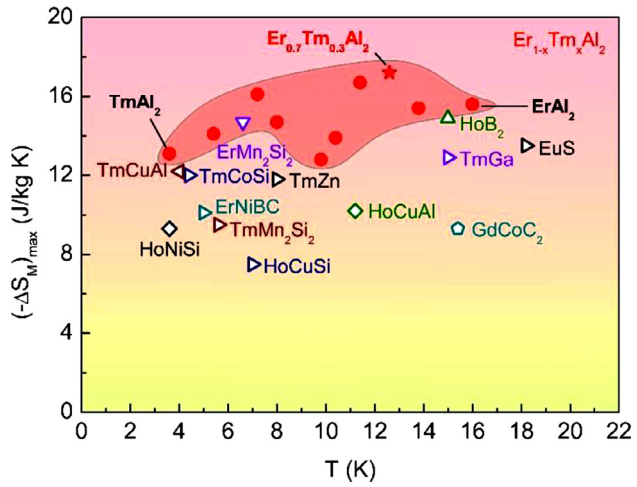

Fig. 6. Comparison of the field change of 0–1 T between $Er_{1-x}Tm_xAl_2$ compounds and other reported low-temperature magnetic materials with large/giant low-field MCE.

for $Er_{0.7}Tm_{0.3}Al_2$ compound is much larger than almost all the intermetallic magnetocaloric materials ever reported at the temperatures below 20 K. Another important parameter to evaluate magnetocaloric materials is refrigeration capacity (RC), which is calculated to be 91.5, 190.0, and 501.2 J/kg for 0–1 T, 0–2 T, and 0–5 T for $Er_{0.7}Tm_{0.3}Al_2$ compound, respectively.

As an important MCE parameter to evaluate MCE directly and unambiguously, adiabatic temperature change (ΔT_{ad}) can be calculated based on the heat capacity measurements. Temperature dependence of the zero-field heat capacity for $Er_{0.7}Tm_{0.3}Al_2$ and $Er_{0.6}Tm_{0.4}Al_2$ compounds was shown in Fig. 7(a, b), respectively. First of all, only one obvious λ-shape peak located around 10 K is observed, which is due to the FM-to-PM transition. The peak position is consistent with the Curie temperature obtained from MT curves. Secondly, the asymmetrical shape of the peaks reflects the second-order characteristic of magnetic transitions [19]. Fig. 7(c) and 7(d) presented the ΔT_{ad} as a function of temperature under the field changes from 0–1 T to 0–7 T for $Er_{0.7}Tm_{0.3}Al_2$ and $Er_{0.6}Tm_{0.4}Al_2$ compounds, respectively, which were calculated by using the indirect method [15] with the equation of $\Delta T_{ad}(T) = T(S, H_f) - T(S, H_i)$. Here, H_f and H_i are the final and initial magnetic fields respectively, and S is the total entropy of the system. The maximum values of ΔT_{ad} ($(\Delta T_{ad})_{max}$) for $Er_{0.7}Tm_{0.3}Al_2$ and $Er_{0.6}Tm_{0.4}Al_2$ were calculated as 4.13, 6.87, 12.43 K and 4.06, 6.91 12.73 K under the field changes of 0–1 T, 0–2 T and 0–5 T, respectively. The $(\Delta T_{ad})_{max}$ shows a relatively small difference at various field changes between these two compounds. The possible reason is that the $(-\Delta S_M)_{max}$ and T_C are both close to each other. It is worth mentioning that the values of $(\Delta T_{ad})_{max}$ for $Er_{0.7}Tm_{0.3}Al_2$ and $Er_{0.6}Tm_{0.4}Al_2$ are both distinctly higher than those of typical magnetocaloric materials such as HoB_2 (3.4, 6.0, and 12.0 K) and TmGa (3.2, 5.0, and 9.1 K) under the field changes of 0–1 T, 0–2 T, and 0–5 T, respectively. Although the value of $(\Delta T_{ad})_{max}$ for $Er_{0.7}Tm_{0.3}Al_2$ is slightly smaller than that of $ErMn_2Si_2$ for 0–5 T, it is almost 1.7 times larger than that of $ErMn_2Si_2$ for 0–1 T. Based on overall considerations on MCE parameters including not only $(-\Delta S_M)_{max}$ but also $(\Delta T_{ad})_{max}$, $Er_{0.7}Tm_{0.3}Al_2$ compound exhibits great competitiveness among the well-known low-temperature magnetic refrigerants. In other words, the $Er_{0.7}Tm_{0.3}Al_2$ compound could be a high-performance candidate for magnetic cooling at low temperatures between liquid helium and liquid hydrogen temperatures. The excellent low-field MCE performance of the $Er_{0.7}Tm_{0.3}Al_2$ compound originates from the FM-ordered magnetic structure and low saturation field.

The characteristic of second-order magnetic transition is of great importance to the applications of magnetocaloric materials. For the $Er_{1-x}Tm_xAl_2$ ($0 \le x \le 1$) system, the feature of second-order magnetic transition around T_C was discussed on basis of the plots shown in Fig. 4(d). Indeed, the same conclusion was obtained in the parent $ErAl_2$ compound [19]. Several kinds of methods have been developed theoretically and experimentally to confirm the characteristic of magnetic transitions [47,48]. To further investigate the type of FM-to-PM magnetic transitions, three alternative methods have been adopted. Firstly, the quantitative criterion of exponent n following power-law expression $|\Delta S_M| \propto H^n$ was investigated [49]. Temperature dependence of exponent n was presented in Fig. 8(a, d) for $Er_{0.7}Tm_{0.3}Al_2$ and $Er_{0.6}Tm_{0.4}Al_2$ compounds and the magnitude of the magnetic field used here was 7 T. No overshoot of n larger than 2 is observed in the whole temperature range below 50 K and only a minimum of n can be observed at ~11.5 K for $Er_{0.7}Tm_{0.3}Al_2$ and ~10.5 K for $Er_{0.6}Tm_{0.4}Al_2$, which is close to their Curie temperatures (12.6 K and 11.4 K), respectively. With further increasing temperature above T_C, n goes up to a plateau near the value of 2, indicating the second-order characteristic of FM-to-PM transition. Secondly, the rescaled universal $-\Delta S_M$ curves under different field changes for $Er_{1-x}Tm_xAl_2$ compounds were also investigated. In this method, $-\Delta S_M$ was normalized as $-\Delta S_M(T, H)/(-\Delta S_M)_{max}$ and temperature was rescaled as Eq. (2) [47]:

$$\theta = \begin{cases} -\dfrac{T - T_C}{T_{r1} - T_C} & (T \le T_C) \\ \dfrac{T - T_C}{T_{r2} - T_C} & (T > T_C) \end{cases} \quad (2)$$

where T_{r1} and T_{r2} are the reference temperatures corresponding to certain $(-\Delta S_M)$ and it is usually selected as half of $(-\Delta S_M)_{max}$. The normalized curves under the field changes from 0–1 T to 0–7 T for $Er_{0.7}Tm_{0.3}Al_2$ and $Er_{0.6}Tm_{0.4}Al_2$ compounds were shown in Fig. 8(b, e). The rescaled $(-\Delta S_M)$ curves collapse on each other very well, indicating a second-order magnetic transition for both of them [48]. Thirdly, the linear relationship between $(-\Delta S_M)_{max}$ and $(\mu_0 H)^{2/3}$ was predicted on basis of mean-field theory for the second-order magnetic transition system [26] and it can also be used to confirm the type of magnetic transitions. The dependences of $(-\Delta S_M)_{max}$ and $(\mu_0 H)^{2/3}$ were plotted in Fig. 8(c, f). It can be clearly seen that $(-\Delta S_M)_{max}$ almost obeys the linear relationship with $(\mu_0 H)^{2/3}$ for $Er_{0.7}Tm_{0.3}Al_2$ and $Er_{0.6}Tm_{0.4}Al_2$ samples, showing another typical feature of second-order magnetic transition. Based on the above analysis, it is reasonable to conclude that the FM-to-PM magnetic transition is an irrefutable second-order type for $Er_{1-x}Tm_xAl_2$ compounds, which is in accordance with the parent $ErAl_2$ compound. Considering that magnetocaloric materials of second-order magnetic transition are usually accompanied by negligible magnetic and thermal hysteresis, the $Er_{0.7}Tm_{0.3}Al_2$ compound is more competitive and more valuable for the practical applications of low-temperature magnetic refrigeration.

4. Conclusion

In summary, the influence of Tm substitution on the magnetic properties and magnetocaloric effect in $Er_{1-x}Tm_xAl_2$ ($0 \le x \le 1$) systems was systematically investigated. Curie temperature was effectively adjusted by varying Tm concentration and the working temperature of $Er_{1-x}Tm_xAl_2$ compounds was decreased from 16.0 K to 3.6 K monotonically. Magnetic structure with rare earth atomic magnetic moments arranged along ⟨111⟩ direction was confirmed for the first time on basis of neutron powder diffraction experiments. Giant MCE was obtained for several components with large $(-\Delta S_M)_{max}$ more than 15.0 and 22.5 J/(kg K) under the relatively low field changes such as 0–1 T and 0–2 T. Particularly, $Er_{0.7}Tm_{0.3}Al_2$ compound shows the largest $(-\Delta S_M)_{max}$ for 0–1 T

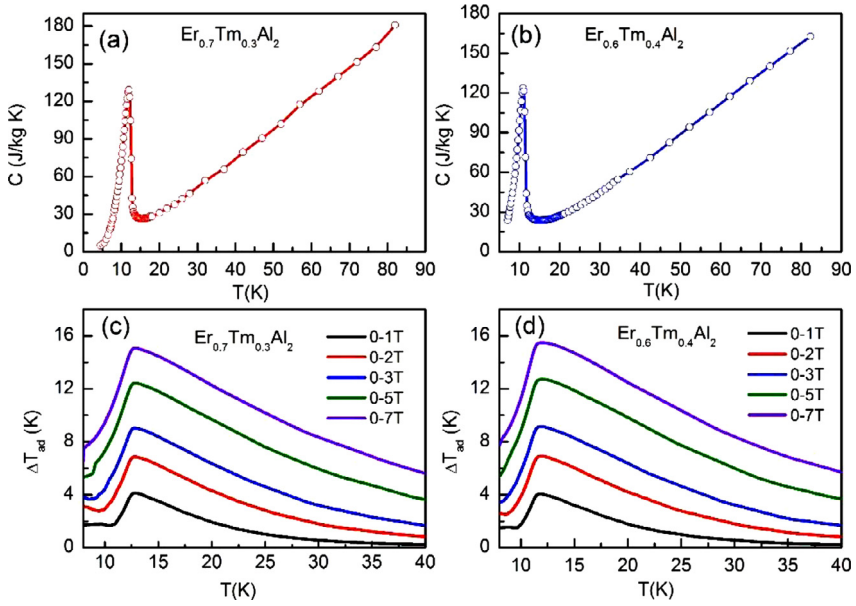

Fig. 7. (a) Zero-field specific heat of $Er_{0.7}Tm_{0.3}Al_2$ and (b) $Er_{0.6}Tm_{0.4}Al_2$ compounds, respectively. (c) Temperature dependences of adiabatic temperature change (ΔT_{ad}) under different field changes for $Er_{0.7}Tm_{0.3}Al_2$ and (d) $Er_{0.6}Tm_{0.4}Al_2$ compounds, respectively.

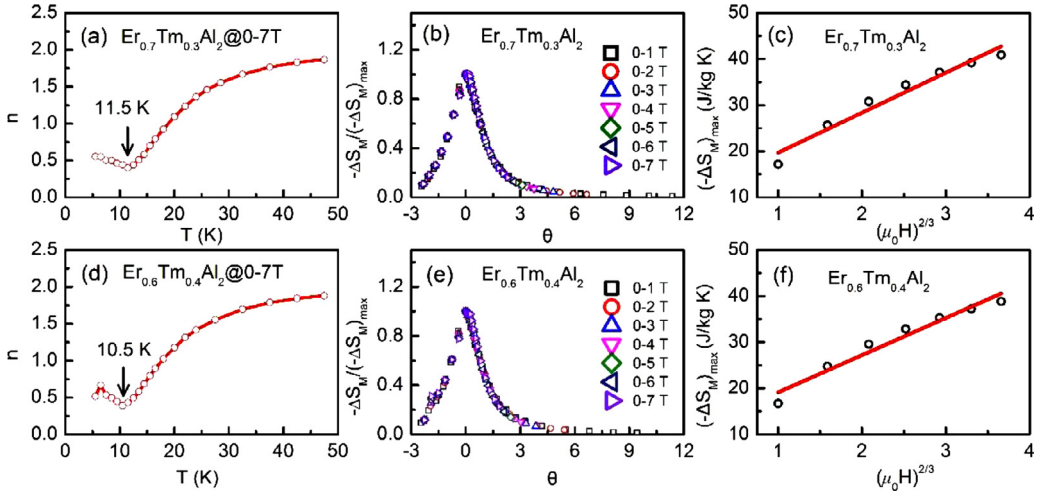

Fig. 8. Temperature dependence of critical exponent n for $Er_{0.7}Tm_{0.3}Al_2$ (a) and $Er_{0.6}Tm_{0.4}Al_2$ (d) compounds. Rescaled ($-\Delta S_M$) curves for $Er_{0.7}Tm_{0.3}Al_2$ (b) and for $Er_{0.6}Tm_{0.4}Al_2$ (e) compounds. Linear relationship between $(-\Delta S_M)_{max}$ and $(\mu_0 H)^{2/3}$ for $Er_{0.7}Tm_{0.3}Al_2$ (c) and $Er_{0.6}Tm_{0.4}Al_2$ (f) compounds.

with the value of 17.2 J/(kg K) among the ever reported low temperature intermetallic magnetocaloric materials. Moreover, the $(\Delta T_{ad})_{max}$ is determined to be 4.13 K and 6.87 K for 0–1 T and 0–2 T, respectively. The excellent low-field MCE performance originates from the FM-ordered magnetic structure and low saturation field. The magnetic transition of $Er_{1-x}Tm_xAl_2$ compounds was confirmed to be of second order according to Arrott plots, exponent n, rescaled universal ($-\Delta S_M$) curves, and mean field theory. The excellent balanced MCE performance with considerable $(-\Delta S_M)_{max}$ and $(\Delta T_{ad})_{max}$ indicates that the $Er_{0.7}Tm_{0.3}Al_2$ compound will be a promising candidate magnetocaloric material and suitable for low-temperature magnetic refrigeration applications.

Declaration of Competing Interest

The authors declare that they have no known competing financial interests or personal relationships that could have appeared to influence the work reported in this paper.

Acknowledgments

This work was financially supported by the National Key Research and Development Program of China (Nos. 2021YFB3501202 and 2019YFB2005800), the Science Center of the National Science Foundation of China (No. 52088101), the National Natural Science Foundation of China (Nos. 51871019, 52171170, 52130103, 51961145305, 51971026, and 52171169), the Beijing Natural Science Foundation Key Program (Grant Nos. Z190007 and Z200007), and "111 Project" (No. B170003).

References

[1] C. Zimm, A. Jastrab, A. Sternberg, V.K. Pecharsky, K.A. Gschneidner, M. Osborne, I. Anderson, Adv. Cryog. Eng. 43 (1997) 1759–1766.
[2] B.G. Shen, J.R. Sun, F.X. Hu, H.W. Zhang, Z.H. Cheng, Adv. Mater. 21 (2009) 4545–4564.
[3] V. Franco, J.S. Blazquez, J.J. Ipus, J.Y. Law, L.M. Moreno-Ramirez, A. Conde, Prog. Mater. Sci. 93 (2018) 112–232.
[4] N.A. de Oliveira, P.J. von Ranke, Phys. Rep. 489 (2010) 89–159.

[5] L.W. Li, M. Yan, J. Alloy. Compd. 823 (2020) 153810.
[6] P.B. de Castro, K. Terashima, T.D. Yamamoto, Z.F. Hou, S. Iwasaki, R. Matsumoto, S. Adachi, Y. Saito, P. Song, H. Takeya, Y. Takano, NPG Asia Mater. 12 (2020) 35.
[7] D.X. Li, T. Yamamura, S. Nimori, Y. Homma, F. Honda, Y. Haga, D. Aoki, Solid State Commum. 193 (2014) 6–10.
[8] S.X. Yang, X.Q. Zheng, W.Y. Yang, J.W. Xu, J. Liu, L. Xi, H. Zhang, L.C. Wang, Z.Y. Xu, J.Y. Zhang, Y.F. Wu, X.B. Ma, D.F. Chen, J.B. Yang, S.G. Wang, B.G. Shen, Phy. Rev. B 102 (2020) 174441.
[9] X.Q. Zheng, B. Zhang, H. Wu, F.X. Hu, Q.Z. Huang, B.G. Shen, J. Appl. Phys. 120 (2016) 163907.
[10] Z.J. Mo, J. Shen, L.Q. Yan, J.F. Wu, L.C. Wang, J. Lin, C.C. Tang, B.G. Shen, Appl. Phys. Lett. 102 (2013) 192407.
[11] J.W. Xu, X.Q. Zheng, S.X. Yang, L. Xi, J.Y. Zhang, Y.F. Wu, S.G. Wang, J. Liu, L.C. Wang, Z.Y. Xu, B.G. Shen, J. Alloy. Compd. 843 (2020) 155930.
[12] E. Bykov, W. Liu, K. Skokov, F. Scheibel, O. Gutfleisch, S. Taskaev, V. Khovaylo, D. Plakhotskiy, C.S. Mejia, J. Wosnitza, T. Gottschall, Phys. Rev. Mater. 5 (2021) 095405.
[13] J.C.P. Campoy, E.J.R. Plaza, A.A. Coelho, S. Gama, Phy. Rev. B 74 (2006) 134410.
[14] K.A. Gschneidner, V.K. Pecharsky, S.K. Malik, Adv. Cryog. Eng. Mater. 42 (1996) 475–483.
[15] V.K. Pecharsky, K.A. Gschneidner, J. Appl. Phys. 86 (1999) 565–575.
[16] A.K. Pathak, K.A. Gschneidner, V.K. Pecharsky, J. Appl. Phys. 117 (2015) 17C107.
[17] M. Khan, K.A. Gschneidner, V.K. Pecharsky, J. Appl. Phys. 107 (2010) 09A904.
[18] A.L. Lima, K.A. Gschneidner, V.K. Pecharsky, A.O. Pecharsky, Phy. Rev. B 68 (2003) 134409.
[19] M. Khan, K.A. Gschneidner, V.K. Pecharsky, J. Magn. Magn. Mater. 324 (2012) 1381–1384.
[20] M. Khan, K.A. Gschneidner, V.K. Pecharsky, Phy. Rev. B 80 (2009) 224408.
[21] Y. Mudryk, B.P. Alho, P.O. Ribeiro, V.K. Pecharsky, Metals (Basel) 10 (2020) 1662.
[22] L.A. Gil, J.C.P. Campoy, E.J.R. Plaza, M.V. de Souza, J. Magn. Magn. Mater. 409 (2016) 45–49.
[23] P.O. Ribeiro, B.P. Alho, R.S. de Oliveira, E.P. Nobrega, V.S.R. de Sousa, P.J. von Ranke, Y. Mudryk, V.K. Pecharsky, J. Alloy. Compd. 858 (2021) 157682.
[24] P.J. von Ranke, V.K. Pecharsky, K.A. Gschneidner Jr, Phy. Rev. B 58 (1998) 12110.
[25] J. Ćwik, Y. Koshkid'ko, K. Nenkov, A. Mikhailova, M. Malecka, T. Romanova, N. Kolchugina, N.A. de Oliveira, Phy. Rev. B 103 (2021) 214429.
[26] H. Oesterreicher, F.T. Parker, J. Appl. Phys. 55 (1984) 4334–4338.
[27] X.Q. Zheng, J. Chen, L.C. Wang, R.R. Wu, F.X. Hu, J.R. Sun, B.G. Shen, J. Appl. Phys. 115 (2014) 17A905.
[28] J.L. Sánchez Llamazares, J. Zamora, C.F. Sanchez-Valdes, P. Alvarez-Alonso, J. Alloy. Compd. 831 (2020) 154779.
[29] A.V.G. Chizmeshya, M.R. Bauer, J. Kouvetakis, Chem. Mater. 15 (2003) 2511–2519.
[30] K.A. Gschneidner, G.H. Vineyard, J. Appl. Phys. 33 (1962) 3444–3450.
[31] M.V. de Souza, J.A. da Silva, L.S. Silva, J. Magn. Magn. Mater. 433 (2017) 248–253.
[32] P.O. Ribeiro, B.P. Alho, T.S.T. Alvarenga, E.P. Nobrega, V.S.R. de Sousa, A.M.G. Carvalho, A. Caldas, P.H.O. Lopes, P.J. von Ranke, J. Magn. Magn. Mater. 442 (2017) 265–269.
[33] J.L. Wang, C. Marquina, M.R. Ibarra, G.H. Wu, Phy. Rev. B 73 (2006) 094436.
[34] J.Y. Li, Y.F. Liu, X. Lu, Y.F. Zhang, J.P. Guo, M.X. Zhang, J. Liu, J. Alloy. Compd. 864 (2021) 158757.
[35] S.K. Banerjee, Phys. Lett. 12 (1964) 16–17.
[36] A. Fujita, Y. Akamatsu, K. Fukamichi, J. Appl. Phys. 85 (1999) 4756–4758.
[37] V.K. Pecharsky, K.A. Gschneidner, Phys. Rev. Lett. 78 (1997) 4494–4497.
[38] Z.J. Mo, J. Shen, L.Q. Yan, C.C. Tang, J. Lin, J.F. Wu, J.R. Sun, L.C. Wang, X.Q. Zheng, B.G. Shen, Appl. Phys. Lett. 103 (2013) 052409.
[39] L.W. Li, K. Nishimura, W.D. Hutchison, Z.H. Qian, D.X. Huo, T. NamiKi, Appl. Phys. Lett. 100 (2012) 152403.
[40] L.W. Li, M. Kadonaga, D.X. Huo, Z.H. Qian, T. Namiki, K. Nishimura, Appl. Phys. Lett. 101 (2012) 122401.
[41] L.C. Wang, Q.Y. Dong, Z.J. Mo, Z.Y. Xu, F.X. Hu, J.R. Sun, B.G. Shen, J. Appl. Phys. 114 (2013) 163915.
[42] J. Chen, B.G. Shen, Q.Y. Dong, F.X. Hu, J.R. Sun, Appl. Phys. Lett. 96 (2010) 152501.
[43] L.J. Meng, C. Xu, Y. Yuan, Y. Qi, S.Q. Zhou, L.W. Li, RSC Adv. 6 (2016) 74765–74768.
[44] L.W. Li, B. Saensunon, W.D. Hutchison, D.X. Huo, K. Nishimura, J. Alloy. Compd. 582 (2014) 670–673.
[45] L.W. Li, Y. Yuan, Y.K. Zhang, T. Namiki, K. Nishimura, R. Pottgen, S.Q. Zhou, Appl. Phys. Lett. 107 (2015) 132405.
[46] H. Zhang, Y.Y. Wu, Y. Long, H.S. Wang, K.X. Zhong, F.X. Hu, J.R. Sun, B.G. Shen, J. Appl. Phys. 116 (2014) 213902.
[47] V. Franco, J.S. Blazquez, A. Conde, Appl. Phys. Lett. 89 (2006) 222512.
[48] V. Franco, J.S. Blazquez, B. Ingale, A. Conde, Ann. Rev. Mater. Res. 42 (2012) 305–342.
[49] J.Y. Law, V. Franco, L.M. Moreno-Ramirez, A. Conde, D.Y. Karpenkov, I. Radulov, K.P. Skokov, O. Gutfleisch, Nat. Commun. 9 (2018) 2680.